EES Solar

ROYAL SOCIETY OF CHEMISTRY

PAPER

View Article Online
View Journal | View Issue

Cite this: *EES Sol.*, 2025, **1**, 554

More junctions is not always better: mapping optimal bandgap partners for tandem and triple-junction solar cells

Carlos Iván Cabrera [a] and Osbel Almora *[b]

The detailed balance (DB) efficiency limit serves as a fundamental framework for evaluating the potential power conversion efficiency (PCE) of photovoltaic (PV) devices. While single-junction (1J) solar cells exhibit a theoretical efficiency peak of ~30% under standard illumination conditions, multijunction architectures such as tandem (2J) and triple-junction (3J) solar cells can exceed 44% and 50%, respectively. This work systematically explores the DB efficiency limits of multijunction solar cells, incorporating radiative coupling effects and optimizing bandgap partner selections. Our contour plot analyses reveal the impact of bandgap partner choices on efficiency gains and highlight key design trade-offs in junction count and sub-cell configuration. We find that while optimized 3J devices theoretically outperform their 2J and 1J counterparts, experimental reports often fall short of these theoretical limits due to suboptimal bandgap partner selection, particularly in all-perovskite systems. The study underscores the importance of achieving at least a 5% efficiency gain per added junction to justify increased complexity in 2J and 3J devices. Furthermore, we discuss how radiative coupling can enhance multijunction device performance, particularly for tandem configurations below the optimal bandgap partner line. Our findings provide insights for optimizing PV device design, balancing efficiency improvements with practical material and fabrication constraints.

Received 13th July 2025
Accepted 16th July 2025

DOI: 10.1039/d5el00118h

rsc.li/EESSolar

Broader context

As the photovoltaic field progresses toward increasingly complex multijunction architectures, one critical yet often underestimated factor is the selection of optimal bandgap combinations across sub-cells. While significant effort is directed toward material development, interfacial engineering, and device stability, many advanced tandem and triple-junction designs still face performance limitations due to suboptimal bandgap pairing. This study provides a clear theoretical benchmark, based on detailed balance and radiative coupling analyses, to assess multijunction device designs. By recommending a practical empirical threshold of >5% theoretical efficiency gain per added junction and systematically mapping optimal bandgap regions, this work offers a clear benchmark and decision-making tool to guide early-stage material design choices, to address whether the added complexity is justified by a sufficient theoretical efficiency gain, ultimately supporting more efficient and targeted innovation in next-generation photovoltaics. This study focuses on informing where to best direct development efforts to avoid costly pursuits of inherently limited device architectures.

1. Introduction

The detailed balance (DB) limit of power conversion efficiency (PCE) of p–n homojunction solar cells[1] is one of the foundational models[2] for evaluating the potential of photovoltaic (PV) materials and devices. This model assumes an ideal scenario in which no trap-assisted non-radiative recombination occurs, allowing the device to behave as a perfect blackbody radiator. In this context, the recombination of electrons and holes is solely radiative and is temperature-dependent. However, in addition to the cell temperature, the bandgap energy (E_g) of the semiconductor absorber governs the two primary energy loss mechanisms in the DB limit: the non-absorption of sub-bandgap photons and the thermalization of above-bandgap photons.[3]

Additional losses, such as the Boltzmann, Carnot[4] and emission losses,[5–7] are present, but optimizing E_g remains the most effective strategy for enhancing efficiency. A smaller E_g increases the absorption range leading to an improvement in the photocurrent. However, this comes at the cost of reduced photovoltage, creating a tradeoff that impacts the output power density (P_{out}). For single-junction (1J) solar cells under 1-sun illumination, the PCE peaks at ~30% within the range $0.93 < E_g < 1.61$ eV.[8] This implies that single-junction devices lose approximately 70% of the incident power density (P_{in}), a fraction that can be even higher for excitonic solar cells,[9] transparent[10,11] or color[12] applications.

[a]*Unidad Académica de Ciencia y Tecnología de la Luz y la Materia, Universidad Autónoma de Zacatecas, Zacatecas, 98160, Mexico*
[b]*Department of Electronic, Electric and Automatic Engineering, Universitat Rovira i Virgili, 43007 Tarragona, Spain. E-mail: osbel.almora@urv.cat*

Such inefficiencies have driven research into advanced photon management strategies, including intermediate band,[13,14] impurity PV effect,[15] multiple exciton generation,[16] singlet fission[17,18] and multijunction solar cells.[19] Among these, the multijunction approach stands out as the leading alternative due to its high PCE limit (see Table 1) and relatively straightforward design. Experimental results have demonstrated PCE values exceeding 30% for multijunction devices (see Fig. 1a).[20,21]

The conventional multijunction design involves a planar arrangement of single-junction solar cells with progressively smaller bandgaps. This configuration minimizes losses from sub-bandgap photon non-absorption and above-bandgap photon thermalization. Fig. 1b provides experimental data on the top sub-cell bandgap (E_g^{top}) as a function of the bottom sub-cell bandgap (E_g^{bottom}), with $E_g^{top} > E_g^{bottom}$. Fig. 1c complements this by illustrating the simplest tandem (two-junction, 2J) solar cell design, detailing the absorbed and transmitted spectra, radiative-coupling luminescence,[19,22] and equivalent circuit. For the triple-junction (3J) devices, a middle sub-cell is considered with an absorber material bandgap value (E_g^{mid}) in between those of the top and bottom sub-cells ($E_g^{top} > E_g^{mid} > E_g^{bottom}$). Moreover, several alternative multijunction structures[23] have been studied, including bifacial,[24–26] step-cell,[27] edge-illumination,[28] PV mirrors,[29] area de-coupled double tandem photovoltaic modules,[30] and hybrid parallel/series devices.[31,32]

The highest reported PCE values for monolithic two-terminal (2T) tandem and triple-junction (3J) devices (Fig. 1a) are predominantly achieved with GaAs- and silicon-based solar cells. This may appear unsurprising,[37] given the technological maturity of these material technologies and the proximity of their E_g^{bottom} values to the well-established absolute optimal bandgap partner (OBP) values (see Table 1). Notably, silicon-perovskite tandem solar cells have garnered significant attention in the literature for identifying OBP pairings within the framework of the DB efficiency limit.[35,38–43]

However, Fig. 1a also highlights several of "record" PCE values for multijunction devices with E_g^{bottom} similar to silicon, yet these efficiencies remain below the best-performing single-junction devices, and in some cases, even below the best single-junction devices made from their respective absorber materials. This disparity becomes even more pronounced for multijunction designs with higher E_g^{bottom} raising questions about the rationale behind some proposed designs. It appears that certain state-of-the-art multijunction reports may emphasize material availability and fabrication expertise over a theoretical assessment of their optimization potential.

If theoretical optimization were the primary driver, one might expect clustering within "bandgap partners" maps around optimal values. Yet, as shown in Fig. 1c, a wide range of E_g^{top} values, spanning up to ~400 meV, is observed for certain E_g^{bottom} values. This inconsistency is particularly stark for perovskite-based triple-junction and organic multijunction solar cells,[44] which significantly underperform compared to their tandem and single-junction counterparts.

These observations prompt critical questions: Do the lower efficiencies in multijunction devices stem from fabrication challenges that could be resolved with further research, or are they rooted in fundamental design flaws, such as poor bandgap partner selection? Moreover, to what extent it is advantageous to increase the number of junctions based solely on the

Table 1 Literature values of maximum power conversion efficiency under 1 sun AM1.5G illumination for monolithic (2 terminal) multijunction solar cells

E_g^{bottom} (eV)	E_g^{mid} (eV)	E_g^{top} (eV)	PCE (%)	Comments	Ref.
0.94	—	1.64	44.1 (44.3)[a]	2J; 1996	19
0.94	—	1.61	45.3	2J; 300 K; 2002	33
0.94	—	1.60	45.7	2J; 2008	34
0.95	—	1.61	45.7	2J, 300 K; $0.5 < E_g^{bottom} < 1.2$ eV; $1.2 < E_g^{top} <$ 2.4 eV; 2010	16
0.90	—	1.60	44.0	2J; $0.5 < E_g^{bottom} < 1.2$ eV; $1.2 < E_g^{top} <$ 2.0 eV; 2019	35
0.95	—	1.60	45.5	2J, 298.15 K; no radiative coupling; $0.8 < E_g^{bottom} < 1.3$ eV; $1.4 < E_g^{top} < 2.0$ eV; $J_{sc} =$ 25.5 mA cm^{-2}; $V_{oc} = 2.029$ V; 2021	36
0.96	—	1.61	44.9	2J; 300 K, 2025	This work
0.71	1.16	1.83	49.7 (50.1)[a]	3J; 1996	19
0.93	1.37	1.91	51.2	3J; 300 K; 2002	33
0.94	1.37	1.90	51.8	3J; 2008	34
0.93	1.36	1.90	51.4	3J; 300 K; $E_g^{bottom} = 0.93$ eV; $1.1 < E_g^{mid} <$ 1.5 eV; $1.5 < E_g^{top} < 2.3$ eV; 2010	16
0.93	1.37	1.91	51.3	3J; 300 K; $0.4 < E_g^{bottom} < 1.3$ eV; $1.0 <$ $E_g^{mid} < 1.6$ eV; $1.7 < E_g^{top} < 2.1$ eV; 2013	31
0.93	1.37	1.91	51.6[a]	3J; $E_g^{bottom} = 0.93$ eV; $1.15 < E_g^{mid} < 1.8$ eV; $1.8 < E_g^{top} < 2.4$ eV; 2018	32
0.93	1.36	1.90	51.4	3J; 2024	16
0.93	1.36	1.91	50.4	3J; 300 K, 2025	This work

[a] No radiative couple, *i.e.*, assuming reflectors at the interfaces preventing the luminescent radiation to be absorbed by the partner sub-cell(s).

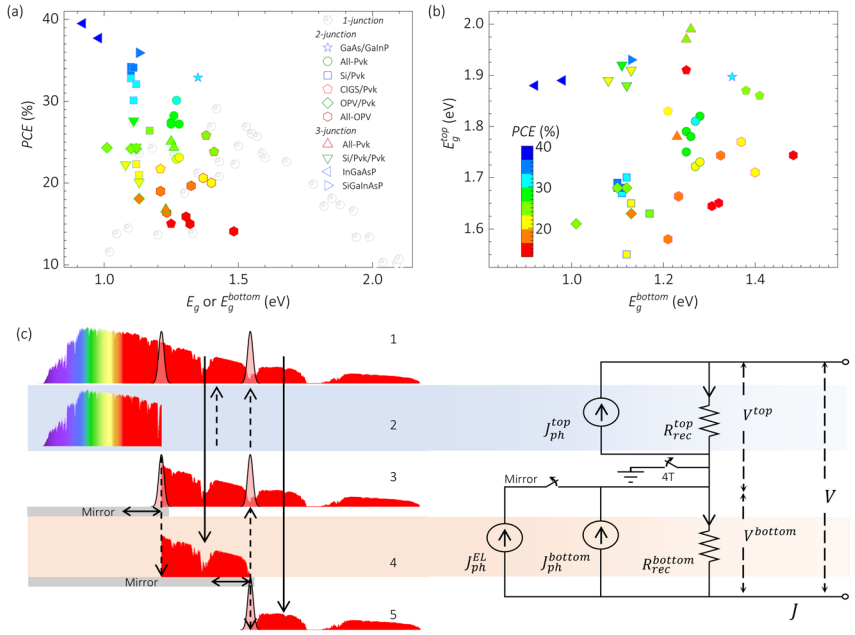

Fig. 1 Monolithic multijunction solar cells: (a) experimental efficiency values and (b) corresponding top- and bottom-sub-cell bandgaps for single, tandem and triple junction devices. Panel (c), schemes the tandem solar cell operating principle and corresponding equivalent circuit specifying the photogenerated current densities (J_{ph}), recombination resistances (R_{rec}) and voltages (V) at the top and the bottom sub-cells, and with/without electroluminescent (EL) contribution due to radiative coupling. The process includes: (1) incidence of a photon flux spectrum at top sub-cell; (2) absorption of photons with energies $>E_g^{top}$ for charge carrier extraction as photocurrent J_{ph}^{top} and recombination due to resistance R_{rec}^{top} at the top sub-cell; (3) transmission of photons with energies $<E_g^{top}$ and emission of luminescent radiation whose half could be reflected at the interface for reabsorption at the top sub-cell, or transmitted for absorption at the bottom sub-cell; (4) absorption of all the photons with energies $>E_g^{bottom}$ at the bottom sub-cell for extraction of charge carriers as electroluminescent photocurrent J_{ph}^{EL} and/or photocurrent J_{ph}^{bottom} due to incident photon flux and the recombination resistance R_{rec}^{bottom}; and (5) emission of luminescent radiation whose half could be reflected at the interface for reabsorption at the bottom sub-cell, or transmitted along with the photons with smaller energies. The symbol colors in (a and b) scale with the efficiency value. The data and legend notation in (a and b) are adapted with permission from Almora *et al.*[21] under a CC BY-NC-ND 4.0 DEED license.

criterion of $E_g^{top} > E_g^{bottom}$? A more nuanced approach to device design may be required to address these issues.

In this work, the DB efficiency limit is calculated within relevant ranges of absorber material bandgap energies of the bottom, middle (in 3J) and top sub-cells for single-junction, tandem and triple-junction solar cells. Not only the optimal bandgap partners are illustrated for each multijunction structure, but also a comparison is offered concerning different junction counts, number of terminals, and management of radiative coupling.[19,22] In addition, practical analyses of other parameters such as the short-circuit current (J_{sc}) and the open-circuit voltage (V_{oc}) are also provided for device performance assessment and comparison of the relative efficiency gain per increase of the number of junctions. Our analyses in contour plot representation allow a more realistic approach to the available semiconductor materials for PV applications and lead to a recommendation in the minimum efficiency gain per junction for the bandgap partner design of multijunction devices.

2. Model

In the multi-junction structure, all sub-cells are assumed to be radiatively coupled to their near neighbors at room temperature (T). The structure is arranged so that the sub-cell bandgaps form a decreasing series ($E_g^{top} \geq E_g^{mid} \geq E_g^{bottom}$). Our calculations are based on the following assumptions.[1] (i) The incident irradiance corresponds to that of the standard solar concentration of 1 sun. (ii) All the sub-cells are considered as black bodies at room temperature. (iii) Each photon with energy greater than that of the material bandgap produces one electron–hole pair. (iv) The device material(s) has (have) infinite carrier mobility. (v) The only electrical loss mechanism considered is the radiative recombination. Our modeling follows similar strategies to those presented in the previous works.[30,39,45]

The current density (J_i) through the i-th sub-cell as a function of the corresponding voltage V_i is given by

$$J_i = J_i^{sc} - J_i^0\left(\exp\left[\frac{qV_i}{k_B T}\right] - 1\right), \quad (1)$$

where k_B is the Boltzmann constant, q is the elementary charge, and $i = 1$ for the top sub-cell, $i = 2$ for the bottom and middle sub-cells in the 2J and 3J devices, respectively, and $i = 3$ for the bottom sub-cell in the 3J cells. The equilibrium black body radiative recombination current J_i^0 is given by

$$J_i^0 = 2q\varphi_i \quad (2)$$

where q is the elementary electron charge, and the black body photon flux is

$$\varphi_i = \frac{2\pi}{c^2}\int_{E_{g_i}/h}^{\infty} \nu^2 \left(\exp\left[\frac{h\nu}{k_B T}\right] - 1\right)^{-1} \mathrm{d}\nu, \quad (3)$$

where ν is the photon frequency, the emission from both the rear and front faces of the sub-cells is considered, c is the speed of light in vacuum, h is the Planck's constant, and E_{g_i} is the bandgap of the i-th sub-cell. An arbitrary sub-cell is irradiated by a fraction of the solar spectrum, as well as the photon fluxes emitted by the preceding and the following sub-cell. The photocurrent, or short-circuit current for the i-th sub-cell with two neighboring sub-cells is given by[45]

$$J_i^{sc} = q\left(\Phi_i + \varphi_{i-1}\exp\left[\frac{qV_{i-1}}{k_B T}\right] + \varphi_{i+1}\exp\left[\frac{qV_{i+1}}{k_B T}\right]\right), \quad (4)$$

where Φ_i is the photon flux incident to the i-th sub-cell from the sun

$$\Phi_i = c\int_{E_{g_i}/h}^{E_{g_{i-1}}/h} \Gamma_{in}(\nu)\frac{\mathrm{d}\nu}{\nu^2} \quad (5)$$

where $\Gamma_{in}(\nu)$ is the solar spectrum AM1.5G. Note that the first (top) sub-cell is illuminated by the sun, and the light emitted by the second (bottom in 2J and middle in 3J) sub-cell, therefore the second term in eqn (4) is discarded. Also, the integration in eqn (5) is made over energies greater than E_{g_i}. On the other hand, the last (bottom) sub-cell of the structure, is not illuminated by any following sub-cell therefore the third term in eqn (4), is discarded.

The total electric power density P generated by the structure is given by

$$P = \sum_{i=1}^{N} V_i J_i \quad (6)$$

and is maximum for $\partial P/\partial J_i = 0$ for i from 1 up to the number of junctions N ($i = 1, 2, 3$ in this work). The (V_i, J_i) solutions for $i = 1, 2, 3$ of this set of equations determines the working points at which the sub-cells have to be operated to extract a maximum of power from the multi-junction structure. Note that for a monolithic multi-junction solar cell, the operating current for all sub-cells is the same ($J_i = J_{i+1} = J$), therefore, the above set of equations simplifies to a single one.

3. Results and conclusions

3.1. Efficiency and radiative coupling in tandem solar cells

The DB efficiency limits for single, tandem and triple junction solar cells are presented in Fig. 2a as a function of the absorber

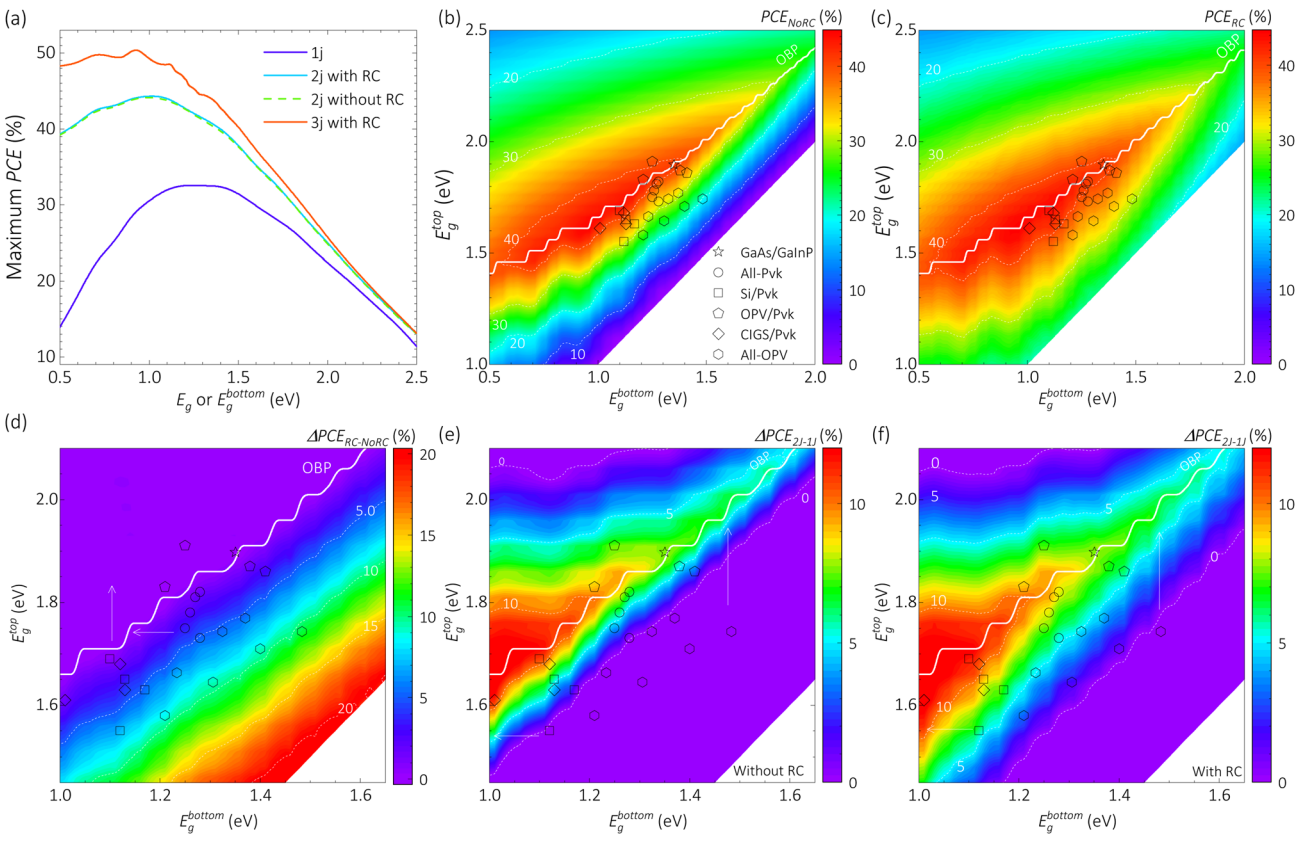

Fig. 2 Radiative coupling analysis between the DB efficiency limits of tandem and single junction solar cells (monolithic, two-terminal). Absolute highest efficiency values as functions of: (a) the bottom sub-cell bandgap for single, two- and triple-junction devices; and the top and bottom sub-cell bandgaps of tandem cells (b) without and (c) with radiative coupling. Difference between the highest efficiencies (d) with–without radiative coupling, and tandem-single junction (e) without and (f) with radiative coupling. Solid lines in (b and c) indicate the optimal bandgap partner configuration corresponding to the highest efficiency values for tandem devices in (a). Symbols correspond to the data in Fig. 1a.

material's bandgap for single-junction devices and the bottom sub-cell's bandgap for tandem and triple-junction solar cells. For tandem (2J) and triple-junction (3J) cells, the maximum efficiencies exceed 44% and 50%, respectively, with optimal bottom sub-cell bandgap values around 0.97 eV and 0.93 eV, as shown in Table 1. Importantly, for each bottom bandgap value multijunction cells outperform their single-junction counterparts in terms of PCE. While this trend suggests that adding more junctions can increase efficiency, such a conclusion can be misleading.

Fig. 2b provides a contour plot of the DB efficiency limits for monolithic tandem devices, illustrating efficiency (PCE_{NoRC}) as a function of the bandgaps of the top and bottom sub-cells without radiative coupling (RC).[19,22] The solid line in the plot identifies the fully optimized bandgap partner combinations (E_g^{bottom}, E_g^{top}) that yield maximum efficiency values, as depicted in Fig. 1a. Experimental data points are overlaid on this plot, showing that only the GaAs/GaInP tandem device aligns with the OBP line, achieving the highest experimental PCE for tandem solar cells. Other tandem configurations, such as silicon-perovskite (Si/Pvk), organic-perovskite (OPV/Pvk), and $CuIn_{1-x}Ga_xSe_2$-perovskite (CIGS/Pvk), are relatively close to the OBP line and fall within the DB efficiency limit region above 40% (red area in Fig. 2b).

However, many devices, including OPV/Pvk, all-perovskite, all-organic, and some Si/Pvk and CIGS/Pvk tandems, were designed with sub-cell bandgap partners that could only achieve efficiencies between 20% and 33% (green-yellow area in Fig. 2b). These efficiencies are lower than those of the best single-junction devices, indicating that sub-OBP design significantly contributes to the poor performance of these tandem solar cells, whose top PCE values range from 15% to 30% (Fig. 1a).

The calculations in Fig. 2b assume perfect radiative decoupling (NoRC) between sub-cells, meaning all excess radiative recombination caused by current matching is reabsorbed within the same sub-cell which emitted. This is illustrated in Fig. 1c, where the mirrors within the structure and the "switched off" electroluminescence photocurrent ($J_{ph,EL}$) in the equivalent circuit prevents the device from operating when $E_g^{bottom} = E_g^{top}$. In this scenario, receives neither transmitted light nor luminescent irradiance, effectively halting its contribution to the device's overall performance. However, real-world devices often feature a transparent recombination layer at the interface between sub-cells, rather than Lambertian reflectors,[46] which could further affect the efficiency of multijunction solar cells.[19,22]

Fig. 2c provides a contour plot of the DB efficiency limits analogous to Fig. 2b, but now incorporating the effect of radiative coupling (RC). Interestingly, the inclusion of RC results in no significant changes along the OBP line (solid line in Fig. 2c), as evidenced by the solid/dashed line comparison of the top efficiency limits with and without RC in Fig. 2a. However, two key differences emerge when comparing the DB efficiency limits with and without RC.

First, for E_g^{top} values above the OBP line, the efficiency limit remains largely unchanged. In this region, luminescent recombination occurs in the bottom sub-cell, and its radiation cannot be absorbed by the top sub-cell because $E_g^{top} > E_g^{bottom}$. Conversely, for $E_{g,top}$ below the OBP line, the efficiency limit increases significantly, enhancing the regions of favorable bandgap partners. Notably, when $E_g^{top} = E_g^{bottom}$, RC enables the bottom sub-cell to generate current from the absorption of radiative recombination from the top sub-cell. This results in DB efficiency limits approximately 10% lower than those of a standalone single-junction device with $E_g = E_g^{bottom}$. This beneficial effect can improve tandem device designs, such as certain all-perovskite 2J cells, which transition from outside the PCE > 40% region without RC to within it when RC is considered (Fig. 2b and c, respectively).

The differences between the DB efficiency limits with and without RC ($\Delta PCE_{RC-NoRC}$) are depicted in Fig. 2d, as a function of the top and bottom sub-cell bandgaps. In this contour plot, the region above the OBP line (purple area) shows negligible or zero differences, while below the OBP line, the difference increases significantly. Moreover, it is shown that most of the reported tandem solar cell efficiencies correspond to bandgap partner designs where optimizing the transparency of the recombination layer between sub-cells could enhance PCE by up to 10%. Additionally, the arrows in Fig. 2d suggest potential routes for reducing dependency on RC by increasing $E_{g,top}$ or decreasing $E_{g,bottom}$.

Finally, Fig. 2e and f present the difference in DB efficiency limits (ΔPCE_{2J-1J}) between tandem solar cells and their corresponding single-junction counterparts with $E_g = E_g^{bottom}$. Both configurations share the same absorption threshold, making this a consistent basis for comparison. Notably, using the single-junction cell with $E_g = E_g^{top}$ as a reference can introduce artefacts, particularly in the range E_g > 1.1 eV where it typically yields lower efficiencies than the bottom-cell counterpart leading to unrealistically high differences (*e.g.*, ΔPCE_{2J-1J} > 12% at OBP line). Positive values of ΔPCE_{2J-1J} indicate that the tandem devices achieve higher efficiencies than the single-junction cells, and *vice versa*. In these contour plots, the green regions represent tandem devices with efficiencies up to 10% higher than their single-junction counterparts, which aligns with most experimental designs reported in the literature. However, some devices, such as all-organic tandems, approach the 0% difference level or even fall into the cyan-blue regions, where single-junction devices outperform tandem cells with the same bottom sub-cell bandgap. This discrepancy is more pronounced without RC, where all-organic tandem devices show efficiency differences of approximately −10% compared to single-junction devices, whereas this improves to near 0% with RC.

Additionally, we calculated the DB efficiency limit for tandem solar cells with radiative coupling in a four-terminal (4T) configuration, which eliminates the requirement for current matching. Note that the RC in 4T configuration only refer to the blackbody radiation of the sub-cells, since no extra recombination is required in the absence of current matching. The results are presented in the contour plot of Fig. 3a, showing the PCE limit as a function of the top and bottom sub-cell bandgaps. The 4T configuration achieves comparable

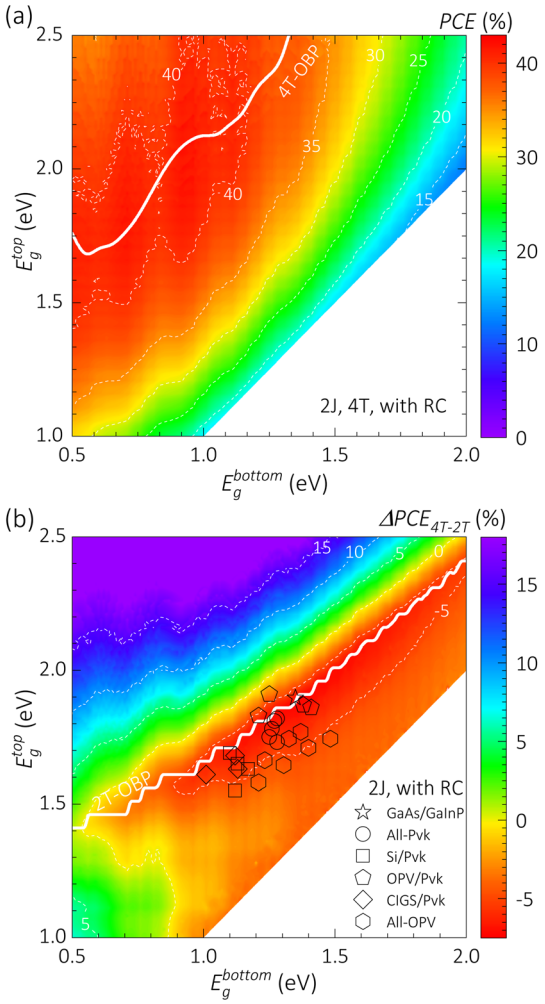

Fig. 3 Four terminal tandem solar cells: (a) DB efficiency limit with radiative coupling and corresponding (b) efficiency difference with respect to the monolithic two-terminal design as a function of the top and bottom sub-cells bandgap. The solid line in (a) corresponds to the optimal bandgap partners in four-terminal configuration. The solid lines and the symbols in (b) correspond to the optimal bandgap partner and experimental reports in the literature for monolithic tandem cells, as presented in Fig. 1b and 2b.

maximum PCE values above 40%, similar to those observed in the two-terminal (2T) configuration. However, achieving these peak efficiencies requires top sub-cell bandgap values near or above 2.0 eV and bottom sub-cell bandgaps below 1.1 eV. These constraints pose significant challenges due to the current limitations in material availability for PV applications.

This issue is further clarified in the contour plot in Fig. 3b, which illustrates the difference (ΔPCE_{4T-2T}) in tandem efficiency limits between the 4T configuration and the monolithic 2T configuration. Positive values of ΔPCE_{4T-2T} indicate that the 4T device archives higher efficiency limit than the corresponding 2T cell, and *vice versa*. The plot also includes the OBP line and representative experimental data from the literature on monolithic cells. Notably, all reported monolithic cells correspond to bandgap partner designs that achieve higher efficiencies in the 2T configuration compared to the 4T configuration. Specifically, most experimental reports indicate efficiency limits approximately 5% higher for 2T designs relative to 4T designs. This underscores the relevance of monolithic tandem research, particularly for bandgap partners below the OBP line.

However, it is also important to consider the role of radiative coupling and the OBP line in 2T efficiency limits, as shown in Fig. 2. While certain strategies to mitigate losses or optimize devices might suggest selecting bandgap partners above the OBP line, caution is needed. Increasing the top sub-cell bandgap can lead to scenarios where the 4T configuration outperforms the 2T configuration. This highlights the nuanced trade-offs in tandem device design and the importance of balancing efficiency gains against material and practical constraints.

Several strategies to optimize radiative coupling in multi-junction solar cells have been explored, though the topic remains largely addressed in theoretical studies and early-stage experiments. Intermediate mirrors, such as air-gap reflectors with antireflection coatings, can selectively reflect luminescent photons while transmitting sub-bandgap light. Ganapati *et al.*[47] reported up to 6% theoretical efficiency gains using this method, though it is generally incompatible with monolithic 2T thin-film devices like perovskite or organic tandems, it has been proven experimentally effective in 4T configurations.[48] Kim *et al.*[49] experimentally assessed nanophotonic intermediate mirrors in Si/perovskite tandems, finding limited performance benefits. Conversely, Nguyen *et al.*[50] measured luminescent coupling with non-destructive photon counting techniques in Si/perovskite tandems suggesting an effective contribution to the current matching. Other approaches include light-trapping and surface texturing, as simulations by Zhu *et al.*[51] showed improved luminescent coupling in triple-junction cells using nanostructured front surfaces. Nevertheless, Zeder *et al.*[52] evaluated texturing to have a minimal effect on RC in perovskite tandems. Moreover, Strandberg[53] proposed transfer coefficients to describe radiative coupling under real conditions, and Bowman *et al.*[54] also developed non-destructive spectroscopic techniques, including cross-sectional luminescence imaging, to evaluate coupling in all-perovskite tandem devices.

3.2. Photocurrent and photovoltage in tandem solar cells

Analyzing performance parameters such as the short-circuit current density (J_{sc}) and the open-circuit voltage (V_{oc}) as functions of sub-cell bandgap energies complements the discussion on efficiency limits (Fig. 2) and provides valuable tools for performance optimization. In Fig. 4a, the solid lines represent the photocurrent values corresponding to the DB efficiency limits in Fig. 2a as a function of the bandgap for single-junction devices and for the bottom sub-cell in tandem and triple-junction devices under the OBP configuration. The symbols indicate illustrative experimental data from the literature.[21] Devices with fewer junctions exhibit higher current levels, and most top-performing devices reported in the literature achieve photocurrents near their theoretical limits. However, single-junction devices are closer to their theoretical limits than

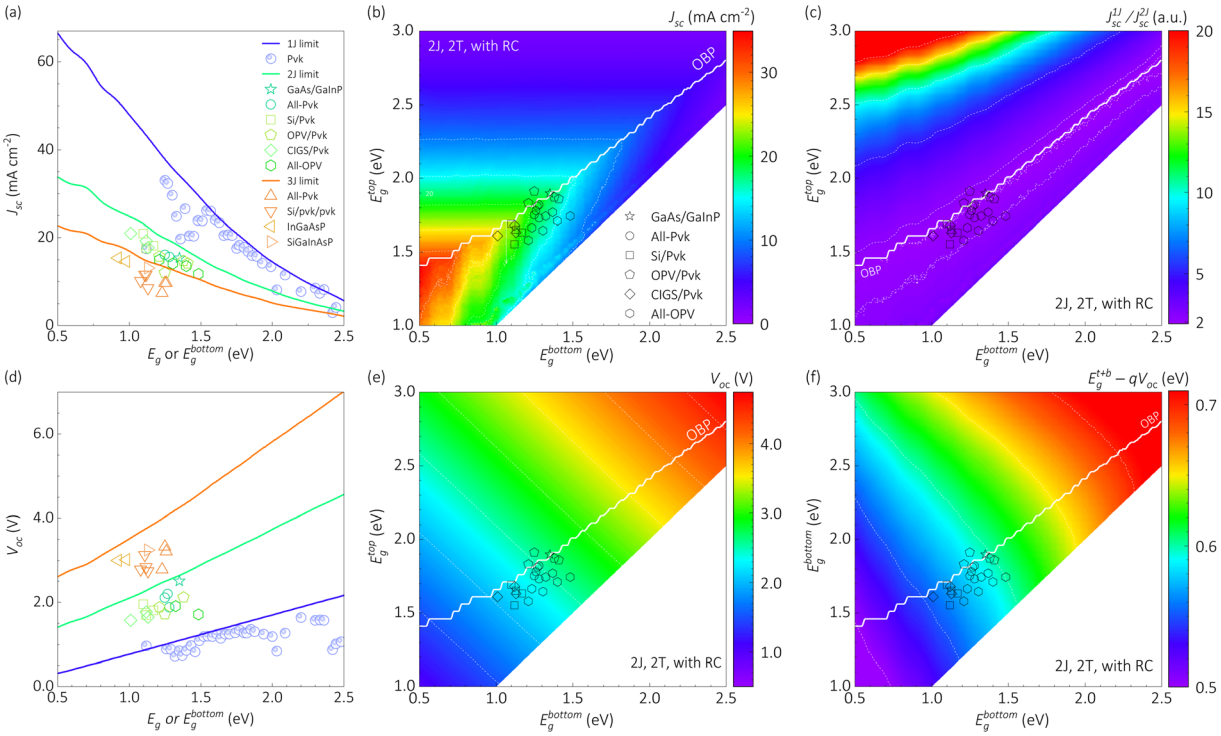

Fig. 4 Photocurrent and photovoltage in the DB efficiency limit for monolithic tandem solar cells with radiative coupling. Panel (a) shows the short-circuit current as a function of the bottom sub-cell bandgap, with the top and middle sub-cells optimized, for single-junction, tandem, and triple-junction devices, as illustrated in Fig. 2a. Panel (b) presents a contour plot of absolute photocurrent values as functions of the top and bottom sub-cell bandgaps, while panel (c) depicts the ratio of the photocurrent with respect to the short-circuit current of the single-junction device. Panel (d) shows the open-circuit voltage as a function of the bottom sub-cell bandgap, with the top and middle sub-cells optimized, again comparing single-junction, tandem, and triple-junction devices as in Fig. 2a. Panel (e) provides a contour plot of absolute photovoltage values as functions of the top and bottom sub-cell bandgaps. Finally, panel (f) illustrates the radiative losses resulting from the energy difference between the sum of sub-cell bandgaps and the DB efficiency limit.

multijunction devices, raising questions about whether this discrepancy is due to suboptimal bandgap partner designs or fabrication challenges.

It is important to note that while the J_{sc} limits for multijunction devices in Fig. 4a represent the maximum achievable photocurrent for each design, they do not reflect the absolute limit for every set of bandgap partners. Fig. 4b provides further insights by presenting the photocurrent as a function of the top and bottom sub-cell bandgaps in the DB efficiency limit for a monolithic tandem solar cell, considering radiative coupling (see PCE limits in Fig. 2c). Above the OBP line (solid line in Fig. 4b), the J_{sc} contour plot exhibits horizontal patterns, as the current is solely determined by the top sub-cell bandgap (J_{ph}^{top}). In this regime, radiative recombination in the bottom sub-cell cannot be absorbed by the top sub-cell since $E_g^{top} > E_g^{bottom}$. Consequently, tandem designs with ($E_g^{top}(E_g^{bottom}) \geq E_g^{OBP}(E_g^{bottom})$) for a given E_g^{bottom} will share the same J_{sc} limit shown in Fig. 4a.

Below the OBP line, the J_{sc} value depends on both top and bottom sub-cell bandgaps. In this case, the bottom sub-cell generates the lower photocurrent (J_{ph}^{bottom}), enabling radiative recombination from the top sub-cell to be reabsorbed by the bottom sub-cell. This interaction creates diagonal patterns in the contour plot, where a decrease in E_g^{top} reduces the J_{sc} limit for a given E_g^{bottom}, as illustrated by the downward vertical arrow in Fig. 4b. This behavior is particularly relevant for optimizing tandem designs, as currently available materials for PV applications may not align with the OBP line. Using an overestimated J_{sc} limit could result in inaccurate performance predictions.

The symbols in Fig. 4b highlight experimental reports on tandem cells, with bandgap coordinates primarily located below the OBP line, showing J_{sc} limits ranging from 15 mA cm^{-2} to 25 mA cm^{-2}. Interestingly, for bandgap partners below the OBP line, the ratio of the short-circuit current for tandem cells (J_{sc}^{2J}) to single-junction cells (J_{sc}^{1J}) is relatively consistent. This ratio, shown in Fig. 4c, ranges from 1.9 at the OBP line to 2.2 below it and increases as E_g^{top} approaches E_g^{bottom}, rarely exceeding 3.0. Above the OBP line, this ratio increases as J_{sc}^{2J} decreases, with higher E_g^{top} values causing the top sub-cell to bottleneck photocurrent generation. However, higher E_g^{top} also leads to greater photovoltage.

Fig. 4d depicts the open-circuit voltage limits (V_{oc}) as functions of the bandgap for single-junction devices and the bottom sub-cell bandgap for tandem and triple-junction devices, with optimized top and middle sub-cells under radiative coupling. These limits, corresponding to the OBP line in the DB model, are shown as solid lines, while symbols represent experimental data from the literature. Similar to J_{sc}, the reported V_{oc} values

align closely with theoretical limits, with single-junction cells achieving the closest reports. Unlike J_{sc} limits, however, the V_{oc} lines in Fig. 4d do not represent the maximum achievable values for multijunction devices; they only relate to the OBP line.

This is better illustrated in Fig. 4e, which shows the V_{oc} limit for tandem cells as increasing with the bandgaps of either the top or bottom sub-cells, regardless of whether the bandgap partner coordinates lie above or below the OBP line. Experimental data in this figure suggest photovoltage limits ranging from 2.0 V to 2.7 V.

Lastly, Fig. 4f illustrates the radiative losses in V_{oc}, calculated as the difference between the sum of the bandgaps of the top and bottom sub-cells ($E_g^{t+b} = E_g^{top} + E_g^{bottom}$) and the quasi-Fermi level splitting at open-circuit conditions (qV_{oc}) in the DB efficiency limit. While these losses generally resemble the V_{oc} limit trends in Fig. 4e, they also highlight the distinct influence of bandgap partner domains above and below the OBP line, particularly for high E_g^{bottom} values, where the impact of E_g^{top} diminishes.

3.3. Efficiency, photocurrent and photovoltage in triple-junction solar cells

Triple-junction solar cells introduce a middle sub-cell that enhances the absorption of incident photon flux while also increasing the number of interfaces and necessitating higher bandgap materials for the top sub-cell. In monolithic devices, considering RC, the bottom sub-cell can absorb radiative recombination from the middle sub-cell, and the middle sub-cell, in turn, can absorb radiative recombination from the top sub-cell.

Fig. 5a illustrates the DB efficiency limit as a function of the top and bottom sub-cell bandgaps for monolithic 3J solar cells with RC, assuming the middle sub-cell bandgap is fully optimized. This middle sub-cell bandgap optimization is further depicted in the contour plot of Fig. 5b. In other words, any 3J device with E_g^{mid} different than that of Fig. 5b as a function of the corresponding E_g^{bottom} and E_g^{top} values would have a smaller DB efficiency limit than the one in Fig. 5a. The solid line in Fig. 5a represents the optimal bandgap partner (OBP) configuration for the efficiency limit, also shown in Fig. 2a, while the symbols correspond to representative literature reports.

Examining experimental results, the highest reported PCE values, with above 39% for InGaAs/GaAs/InGaP devices (see Fig. 1a), correspond to designs with well-matched bandgap partners, which allow efficiency limits exceeding 50% in Fig. 5a. Conversely, the lowest experimental efficiencies among all-perovskite 3J solar cells correspond to bandgap partner designs that permit efficiency limits below 35%. Although these designs theoretically outperform their 1J counterparts (where the 1J cell's bandgap matches the bottom sub-cell of the 3J device), a critical question arises: to what extent can they achieve efficiencies surpassing those of tandem devices with the same top and bottom sub-cell bandgaps?

Fig. 5c presents a comparative contour plot displaying the DB efficiency limit difference (ΔPCE_{3J-1J}) between 3J devices and 1J cells whose bandgap matches that of the bottom sub-cell in

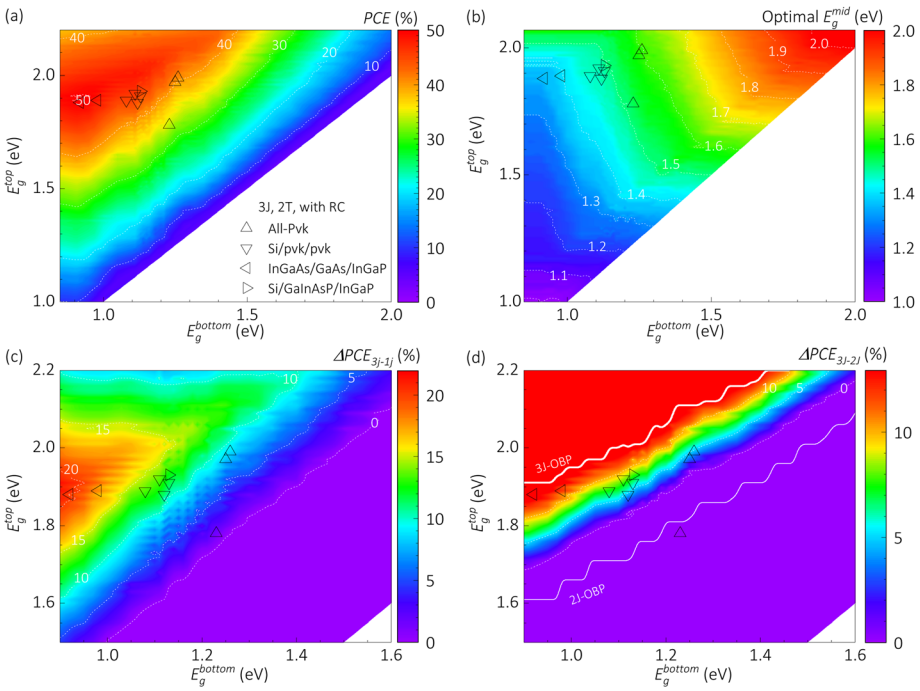

Fig. 5 Triple-junction solar cell DB efficiency limit with radiative coupling as function of top and bottom sub-cell bandgaps: (a) efficiency with optimized middle sub-cell bandgap, (b) optimal middle sub-cell bandgap for efficiency limit in (a), and comparative difference in efficiency limits with respect to those of (c) the single-junction and (d) the monolithic tandem devices. The solid lines in (a) and (d) correspond to the optimal bandgap partners design for the DB efficiency limit in Fig. 2a for 3J (a and d) and 2J (d). Symbols indicate illustrative experimental reports from the literature.[21]

the 3J cell. A positive ΔPCE_{3J-1J} value indicates that the 3J device has a higher PCE limit than the 1J cell, and *vice versa*. The plot reveals that all reported monolithic 3J solar cells (symbols in Fig. 5c) outperform their 1J counterparts. However, while top-efficiency 3J cells with well-optimized bandgap partners exhibit PCE limits exceeding 20% compared to their single-junction equivalents, all-perovskite 3J solar cells achieve only 1% to 10% higher values. This suggests that while perovskite-based 3J devices theoretically surpass 1J devices, their bandgap partner designs are suboptimal. Two key factors contribute to this: (i) the experimental middle sub-cell bandgaps deviate from their theoretical optimal values (Fig. 5b), and (ii) the suboptimal E_g^{bottom} and E_g^{top} design for the all-perovskite 3J solar cells leads to $\Delta PCE_{3J-1J} < 10\%$ in most of the cases. Consequently, our analysis suggests that poor optimization in bandgap partner design is a major reason why perovskite-based 3J solar cells exhibit lower experimental efficiencies than top-performing single-junction devices and achieve only marginal (less than 3%) efficiency gains over the best 1J perovskite solar cells with matching bottom sub-cell bandgaps.

The efficiency gap becomes even more pronounced when comparing 3J devices to tandem cells. Fig. 5d displays the DB efficiency limit difference (ΔPCE_{3J-2J}) between 3J devices and tandem cells with the same bottom sub-cell bandgap. A positive ΔPCE_{3J-2J} value signifies that the 3J device has a higher PCE limit than the 2J cell, and *vice versa*. The majority of reported monolithic 3J cells (symbols in Fig. 5d) outperform their 2J counterparts and fall within the range between the optimal bandgap partner lines for triple-junction (3J-OBP) and tandem (2J-OBP) devices. However, while high-efficiency 3J cells with well-optimized bandgap partners exhibit PCE limits at least 10% higher than their tandem counterparts, all-perovskite 3J cells achieve at most a 5% improvement.

The above analysis highlights a consistent pattern among the highest-performing experimental tandem and triple-junction devices, particularly those developed through systematic optimization: their DB efficiency limits exceed those of comparable single-junction cells by at least 5% and 10%, respectively. From a practical standpoint, this suggests an empirical guideline: multijunction solar cells are recommended to deliver a minimum of 5% DB efficiency gain per added junction relative to a device with fewer junctions. This naturally prompts a critical question: do the efficiency gains justify the added complexity and cost? Factors such as the need for optimal bandgap alignment, more intricate fabrication processes (*e.g.*, additional layers and interfaces), and increased material usage must be carefully weighed when evaluating the real-world value of multijunction architectures.

The empirical rule of achieving a >5% gain in DB efficiency limit, while consistent 2J and 3J devices, requires careful analysis for generalization, especially as the number of junctions increases. The higher the number of sub-cells, the smaller the DB efficiency gain. To formalize this, consider a single junction solar cell with experimental power conversion efficiency PCE_{1J}^{exp} and detailed balance efficiency limit PCE_{1J}^{DB}. This single-junction configuration serves as the bottom sub-cell in a multi-junction device with N sub-cells, whose experimental and DB efficiencies are PCE_{1J}^{exp} and PCE_{NJ}^{DB}, respectively. The experimental junction gain is defined as

$$\eta_{N-1}^{exp} = PCE_{NJ}^{exp} - PCE_{1J}^{exp} \quad (7)$$

and the detailed balance efficiency limit theoretical junction gain is:

$$\eta_{N-1}^{DB} = PCE_{NJ}^{DB} - PCE_{1J}^{DB} \quad (8)$$

Assuming a correlation between the losses in the multi-junction device and those in the single-junction cell (with $E_g = E_g^{bottom}$), we define a proportionality factor γ, which captures the

Table 2 Junction gain and loss analysis on illustrative top-efficiency multijunction literature report, following definitions in equations from (7) to (12) and the DB efficiency limits including radiative coupling

Bottom sub-cell	Si	CIGS	OPV	Pvk	OPV	Pvk	Si
Middle/Top sub-cell	Pvk[56]	Pvk[56]	Pvk[57]	Pvk[58]	OPV[59]	Pvk/Pkv[60]	Pvk/Pvk[61]
N	2	2	2	2	2	3	3
E_g^{bottom} (eV)	1.10	1.09	1.38	1.25	1.37	1.25	1.11
E_g^{mid} (eV)	—	—	—	—	—	1.61	1.58
E_g^{top} (eV)	1.68	1.64	1.87	1.80	1.77	1.97	1.92
PCE_{1J}^{exp} (%)	25.0[a]	23.6	19.0	23.4	18.9	22.0[a]	25.5
PCE_{NJ}^{exp} (%)	34.9	24.6	25.8	29.1	20.6	25.1	27.1
PCE_{1J}^{DB} (%)	32.2	31.9	32.8	32.1	33.0	32.1	32.4
PCE_{NJ}^{DB} (%)	43.4	42.0	39.7	41.2	37.0	39.9	37.7
η_{N-1}^{exp} (%)	9.90	1.00	6.82	5.70	1.70	3.10	1.56
η_{N-1}^{DB} (%)	11.2	10.1	6.90	9.10	4.00	7.80	5.30
δ_{N-1} (%)	1.30	9.10	0.08	3.40	2.30	4.70	3.74
γ (a.u.)	0.44	0.80	0.42	0.54	0.52	0.39	0.44
$\frac{\eta_{N-1}^{DB}}{N-1}$ (%)	11.2	10.1	6.90	9.10	**4.00**	**3.90**	**2.65**

[a] Approximated values considering record 1J PCE reports in the literature.[21]

cumulative losses in the additional $N-1$ sub-cells and the device as a whole. This yields the relation:

$$1-\frac{\mathrm{PCE}_{NJ}^{\mathrm{exp}}}{\mathrm{PCE}_{NJ}^{\mathrm{DB}}}=\gamma N\left(1-\frac{\mathrm{PCE}_{1J}^{\mathrm{exp}}}{\mathrm{PCE}_{1J}^{\mathrm{DB}}}\right) \quad (9)$$

Assuming current matching between the 1J and the multijunction device, a proportionality can be approximated as $\gamma \propto \sum((\Delta V_i/\Delta V_{\mathrm{bottom}})-1)$ where $\Delta V_{\mathrm{bottom}}$ and ΔV_i are the voltage losses at the bottom and ith subsequent sub-cells, respectively. Therefore, the higher the value of γ the higher the photovoltage losses at the top and intermediate sub-cells compared to those at the bottom one. Moreover, rewriting eqn (1) leads to

$$\mathrm{PCE}_{NJ}^{\mathrm{exp}}=\left(1-\gamma N\left(1-\frac{\mathrm{PCE}_{1J}^{\mathrm{exp}}}{\mathrm{PCE}_{1J}^{\mathrm{DB}}}\right)\right)\mathrm{PCE}_{NJ}^{\mathrm{DB}} \quad (10)$$

Subtracting $\mathrm{PCE}_{1J}^{\mathrm{exp}}$ and $\mathrm{PCE}_{1J}^{\mathrm{DB}}$ in both sides of eqn (10), and regrouping terms gives:

$$\eta_{N-1}^{\mathrm{exp}}=\eta_{N-1}^{\mathrm{DB}}-\delta_{N-1} \quad (11)$$

where δ_{N-1} represents the junction-increase efficiency loss, defined as:

$$\delta_{N-1}=\left(\gamma N\ \mathrm{PCE}_{NJ}^{\mathrm{DB}}-\mathrm{PCE}_{1J}^{\mathrm{DB}}\right)\left(1-\frac{\mathrm{PCE}_{1J}^{\mathrm{exp}}}{\mathrm{PCE}_{1J}^{\mathrm{DB}}}\right) \quad (12)$$

This formulation provides a quantitative means to evaluate how much of the theoretical efficiency gain is lost due to cumulative imperfections in real world multijunction integration. As an illustration, Table 2 presents the results of the junction gain and loss analysis, based on the formalism outlined in eqn (7)–(12), applied to a representative set of high-performance multijunction devices reported in the literature. These include emerging technologies such as perovskite and organic sub-cells. Importantly, the previously discussed >5% minimum gain per added junction is quantitatively captured by the metric $\eta_{N-1}^{\mathrm{DB}}/(N-1)$, which exceeds 5% in the best-performing devices and falls below this threshold in the lowest-performing ones. Notably, all of these highest-efficiency perovskite-based 3J solar cells fall into the latter category.

The values of γ presented in Table 2 range from 0.39 to 0.8, which likely indicates significant photovoltage losses in the perovskite layers over silicon and CIGS bottom sub-cells. However, we emphasize that γ alone should be interpreted with caution. While it can serve as a comparative metric for devices with identical bandgap configurations and current-matching conditions, it is not suitable for direct comparisons across different architectures or materials, such as those listed in Table 2. A more robust and physically meaningful interpretation of γ requires a systematic, sub-cell-resolved analysis of photovoltage losses. For example, the approach demonstrated by Thiesbrummel *et al.*[55] offers a valuable reference by combining electroluminescence, photoluminescence, and drift-diffusion simulations to quantify sub-cell contributions to overall voltage deficits.

Importantly, the formalism presented in eqn (7)–(12) is not restricted to the idealized case of fully opaque multijunction devices, with or without radiative coupling. The proposed methodology for junction gain analysis using η_{N-1}^{DB} remains applicable to architectures where material or operational limitations prevent complete opacity of the absorber layers, suitable bandgap materials near the OBP line are unavailable, or parasitic absorption occurs in interfacial layers. In such scenarios, alternative strategies, such as incorporating semitransparent absorbers or adopting horizontal layouts, may be employed to optimize current matching. These configurations can be accommodated by recalculating the DB efficiency limits under revised assumptions, thereby enabling meaningful estimations of η_{N-1}^{DB} within the same analytical framework for each case study.

Fig. 6a presents the photocurrent contour plot as a function of the top and bottom sub-cell bandgaps (provided optimal

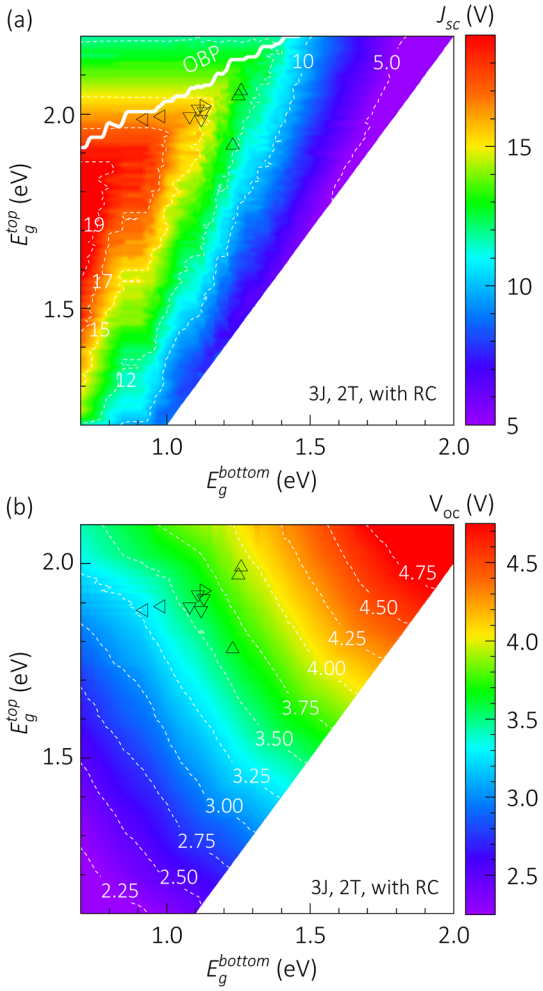

Fig. 6 Short-circuit current density (a) and open-circuit voltage (b) as functions of the bandgaps of the top and bottom sub-cells of a monolithic triple-junction solar cell in the DB efficiency limit considering radiative coupling and optimized middle sub-cell bandgap (see Fig. 5). The solid line in (a) correspond to the optimal bandgap partners design for the DB efficiency limit in Fig. 2a for 3J. Symbols indicate illustrative experimental reports from the literature.[21]

middle bandgap) for the monolithic 3J solar cells in the DB efficiency limit with RC. Similarly to the tandem case in Fig. 4a, a distinction is evident between the cases where the bandgap of the top sub-cell is higher and lower than that of the OBP line, for the same bottom sub-cell bandgap. Above the OBP line the current only depends on E_g^{bottom} and below the OBP line both E_g^{bottom} and E_g^{top} influence the current matching and thus the highest possible photocurrent. Illustrative experimental bandgap partners from the literature are also represented with symbols in Fig. 6a, indicating photocurrent limits between 12 mA cm^{-2} and 17 mA cm^{-2}. Moreover, Fig. 6b presents the analogue photovoltage contour plot for the 3J cells in the DB efficiency limit. In that graph, the same experimental reports from the literature result in photovoltage limits between 3.5 V and nearly 4.0 V, assuming optimal middle sub-cell bandgap values.

The above analysis of the DB radiative limit not only offers a systematic methodology for evaluating optimal bandgap matching in multijunction solar cell designs, but also provides an operational framework for assessing losses due to suboptimal absorption and non-radiative recombination. These are two key factors that prevent experimental devices from reaching their theoretical limits. The differences between experimental and DB efficiency values, as well as the junction gain η_{N-1}^{DB} and loss factor δ_{N-1} introduced in this work, can serve as upper-bound indicators of combined losses. Depending on the available data and system under study, these metrics may help isolate the contribution of non-radiative recombination from that of limited absorption.

4. Conclusions

This study evaluates the detailed balance efficiency limits of single-junction, tandem, and triple-junction solar cells, emphasizing the role of optimal bandgap partner selection and radiative coupling effects. Our findings confirm that while multijunction architectures can theoretically achieve higher efficiencies, many experimental designs fall short due to suboptimal bandgap configurations. The highest efficiency values are observed for devices that align closely with the optimal bandgap partner line, whereas many reported perovskite-based multijunction solar cells deviate from these optimal configurations, resulting in limited efficiency gains.

Radiative coupling plays a significant role in efficiency improvements, particularly for tandem solar cells below the OBP line, where reabsorption of radiative recombination enhances performance. Our results show that considering RC can shift some all-perovskite tandem devices into with suboptimal bandgap matching to the >40% PCE efficiency range, highlighting its importance in device optimization. However, despite the theoretical advantages of adding junctions, many reported 3J perovskite solar cells perform similar or worse that their tandem and single-junction counterparts, raising questions about the practical viability of additional junctions. These findings highlight the need for a more strategic approach to multijunction device design, balancing the theoretical efficiency benefits with practical constraints related to fabrication complexity, material availability, and cost-effectiveness.

Based on current material availability and performance trends, we propose an empirical recommendation of a minimum 5% theoretical efficiency gain per added junction, particularly for devices with up to three junctions. This threshold, derived from DB modeling and consistent with leading lab-scale results, serves as an academic guideline to assess whether the added complexity of multijunction architectures is justified. However, it does not encompass the broader considerations of cost-effectiveness, long-term stability, or manufacturability required for commercial deployment. These factors are context-specific and beyond the scope of this study. Nonetheless, the >5% gain benchmark may be useful for guiding early-stage research and screening promising multijunction designs.

Data availability

The obtained simulation data and the simulation script that support the findings of this study are available from the corresponding author, Osbel Almora, upon reasonable request.

Author contributions

O. A. conceived the idea, directed the overall project, executed several calculations, introduced the gain and loss analyses, and wrote the manuscript. C. I. C. programmed the script for the simulations, executed most of the calculations, and contributed to the discussion and revision of the manuscript.

Conflicts of interest

The authors declare no conflicts of interest.

Acknowledgements

O. A. thanks funding from the Departament de Recerca i Universitats, the Departament d'Acció Climàtica, Alimentació i Agenda Rural and the Fons Climàtic de la Generalitat de Ca talunya for the project Conversion of Energy in Sustainable Chemicals (CESC, 2023 CLIMA 00067).

References

1 W. Shockley and H. J. Queisser, *J. Appl. Phys.*, 1961, **32**, 510–519.
2 A. De Vos, P. T. Landsberg, P. Baruch and J. E. Parrott, *J. Appl. Phys.*, 1993, **74**, 3631–3637.
3 J.-F. Guillemoles, T. Kirchartz, D. Cahen and U. Rau, *Nat. Protoc.*, 2019, **13**, 501–505.
4 P. T. Landsberg and V. Badescu, *J. Phys. D Appl. Phys.*, 2000, **33**, 3004.
5 L. C. Hirst and N. J. Ekins-Daukes, *Prog. Photovoltaics*, 2011, **19**, 286–293.

6 A. S. Garcia and R. Strandberg, *2019 IEEE 46th Photovoltaic Specialists Conference (PVSC)*, Analytical Expressions for Radiative Losses in Solar Cells, 2019.
7 B. Abderrahmane, in *Solar Cells*, ed. A. K. Leonid, IntechOpen, Rijeka, 2015, ch. 2, DOI: 10.5772/58914.
8 S. Rühle, *Sol. Energy*, 2016, **130**, 139–147.
9 K. Seki, A. Furube and Y. Yoshida, *Appl. Phys. Lett.*, 2013, **103**, 253904.
10 R. R. Lunt, *Appl. Phys. Lett.*, 2012, **101**, 043902.
11 K. Forberich, F. Guo, C. Bronnbauer and C. J. Brabec, *Energy Technol.*, 2015, **3**, 1051–1058.
12 J. Halme and P. Mäkinen, *Energy Environ. Sci.*, 2019, **12**, 1274–1285.
13 S. P. Bremner, M. Y. Levy and C. B. Honsberg, *Appl. Phys. Lett.*, 2008, **92**, 171110.
14 T. Nozawa and Y. Arakawa, *Appl. Phys. Lett.*, 2011, **98**, 171108.
15 A. S. Brown and M. A. Green, *J. Appl. Phys.*, 2002, **92**, 1329–1336.
16 J. Lee and C. Honsberg, *2010 35th IEEE Photovoltaic Specialists Conference, Detailed Balance Calculations of Multiple Exciton Generation and Tandem Hybrid Solar Cells*, 2010.
17 M. S. Martinez, A. J. Nozik and M. C. Beard, *J. Chem. Phys.*, 2019, **151**, 114111.
18 M. J. Y. Tayebjee, A. A. Gray-Weale and T. W. Schmidt, *J. Phys. Chem. Lett.*, 2012, **3**, 2749–2754.
19 A. Martí and G. L. Araújo, *Sol. Energy Mater. Sol. Cells*, 1996, **43**, 203–222.
20 M. Yamaguchi, F. Dimroth, J. F. Geisz and N. J. Ekins-Daukes, *J. Appl. Phys.*, 2021, **129**, 240901.
21 O. Almora, G. C. Bazan, C. I. Cabrera, L. A. Castriotta, S. Erten-Ela, K. Forberich, K. Fukuda, F. Guo, J. Hauch, A. W. Y. Ho-Baillie, T. J. Jacobsson, R. A. J. Janssen, T. Kirchartz, R. R. Lunt, X. Mathew, D. B. Mitzi, M. K. Nazeeruddin, J. Nelson, A. F. Nogueira, U. W. Paetzold, B. P. Rand, U. Rau, T. Someya, C. Sprau, L. Vaillant-Roca and C. J. Brabec, *Adv. Energy Mater.*, 2025, **15**, 2404386.
22 Y. Park, B. Zhao and S. Fan, *Nano Lett.*, 2022, **22**, 448–452.
23 X. Wu, B. Li, Z. Zhu, C.-C. Chueh and A. K. Y. Jen, *Chem. Soc. Rev.*, 2021, **50**, 13090–13128.
24 M. A. Alam and M. R. Khan, *Appl. Phys. Lett.*, 2016, **109**, 173504.
25 M. Ryyan Khan and M. A. Alam, *Appl. Phys. Lett.*, 2015, **107**, 223502.
26 A. Onno and Z. C. Holman, *2018 IEEE 7th World Conference on Photovoltaic Energy Conversion (WCPEC) Numerical Analysis of Bifacial Silicon-Based Tandem Devices: Shifts in the Optimum Top-Cell Bandgap with Varying Albedo*, 2018.
27 S. A. Hadi, T. Milakovich, M. Bulsara, E. Polyzoeva, E. A. Fitzgerald, J. L. Hoyt and A. Nayfeh, *2015 IEEE 42nd Photovoltaic Specialist Conference (PVSC), Theoretical Efficiency Limits of a 2 Terminal Dual Junction Step Cell*, 2015.
28 J. E. Parrott, *J. Phys. D: Appl. Phys.*, 1979, **12**, 441.
29 Z. J. Yu, K. C. Fisher, B. M. Wheelwright, R. P. Angel and Z. C. Holman, *IEEE J. Photovoltaics*, 2015, **5**, 1791–1799.
30 R. Strandberg, *Appl. Phys. Lett.*, 2015, **106**, 033902.
31 Y. Ahn, Y. H. Kim and S. I. Kim, *IEEE J. Photovoltaics*, 2013, **3**, 1403–1408.
32 L. Zhang, M. Chen, S. Luo and G. G. Qin, *Renewable Energy*, 2018, **129**, 317–327.
33 A. S. Brown and M. A. Green, *Phys. Educ.*, 2002, **14**, 96–100.
34 S. P. Bremner, M. Y. Levy and C. B. Honsberg, *Prog. Photovoltaics*, 2008, **16**, 225–233.
35 M. I. Hossain, W. Qarony, S. Ma, L. Zeng, D. Knipp and Y. H. Tsang, *Nano–Micro Lett.*, 2019, **11**, 58.
36 J. Chantana, Y. Kawano, T. Nishimura, A. Mavlonov and T. Minemoto, *Opt. Mater.*, 2021, **113**, 110819.
37 L. M. Mansfield, J. J. Cordell, S. Haque, W. E. McMahon and E. L. Warren, *ACS Energy Lett.*, 2025, **10**, 102–106.
38 Z. Yu, M. Leilaeioun and Z. Holman, *Nat. Energy*, 2016, **1**, 16137.
39 M. H. Futscher and B. Ehrler, *ACS Energy Lett.*, 2016, **1**, 863–868.
40 I. Almansouri, A. Ho-Baillie and M. A. Green, *Jpn. J. Appl. Phys.*, 2015, **54**, 08KD04.
41 G. E. Eperon, M. T. Hörantner and H. J. Snaith, *Nat. Rev. Chem.*, 2017, **1**, 0095.
42 M. H. Futscher and B. Ehrler, *ACS Energy Lett.*, 2017, **2**, 2089–2095.
43 M. Heydarian, M. Heydarian, P. Schygulla, S. K. Reichmuth, A. J. Bett, J. Hohl-Ebinger, F. Schindler, M. Hermle, M. C. Schubert, P. S. C. Schulze, J. Borchert and S. W. Glunz, *Energy Environ. Sci.*, 2024, **17**, 1781–1818.
44 K. O. Brinkmann, P. Wang, F. Lang, W. Li, X. Guo, F. Zimmermann, S. Olthof, D. Neher, Y. Hou, M. Stolterfoht, T. Wang, A. B. Djurišić and T. Riedl, *Nat. Rev. Mater.*, 2024, **9**, 202–217.
45 A. D. Vos, *J. Phys. D Appl. Phys.*, 1980, **13**, 839.
46 N. Verena, W. T. Stefan and P. Albert, *J. Photon. Energy*, 2022, **12**, 015502.
47 V. Ganapati, C. S. Ho and E. Yablonovitch, *IEEE J. Photovoltaics*, 2015, **5**, 410–417.
48 R. Mishima, W. Yoshida, H. Ishibashi, H. Tanaka, K. Kishimoto, M. Hino, M. Kanematsu, S. Okamoto, T. Fujimoto, G. Koizumi, H. Uzu, D. Adachi and K. Yamamoto, *Appl. Phys. Lett.*, 2023, **123**, 263510.
49 K. Kim, J. Lee, J. Lee, J.-Y. Kim, H.-S. Lee and S. Lee, *Nanophotonics*, 2025, **14**, 1239–1248.
50 K. Nguyen, O. Fischer, C. Messmer, Y. Zhu, D.-T. Nguyen, A. D. Bui, Z. Hameiri, F. Schindler, M. C. Schubert, H. Shen, K. Weber, K. Catchpole, D. Macdonald and H. T. Nguyen, *Small*, 2024, **20**, 2403461.
51 L. Zhu, Y. Wang, X. Pan and H. Akiyama, *Opt. Express*, 2022, **30**, 35202–35218.
52 S. J. Zeder, B. Blülle, B. Ruhstaller and U. Aeberhard, *APL Energy*, 2025, **3**, 026110.
53 R. Strandberg, *Appl. Phys. Lett.*, 2023, **122**, 253902.
54 A. R. Bowman, F. Lang, Y.-H. Chiang, A. Jiménez-Solano, K. Frohna, G. E. Eperon, E. Ruggeri, M. Abdi-Jalebi, M. Anaya, B. V. Lotsch and S. D. Stranks, *ACS Energy Lett.*, 2021, **6**, 612–620.
55 J. Thiesbrummel, F. Peña-Camargo, K. O. Brinkmann, E. Gutierrez-Partida, F. Yang, J. Warby, S. Albrecht,

D. Neher, T. Riedl, H. J. Snaith, M. Stolterfoht and F. Lang, *Adv. Energy Mater.*, 2023, **13**, 2202674.

56 M. A. Green, E. D. Dunlop, M. Yoshita, N. Kopidakis, K. Bothe, G. Siefer, X. Hao and J. Y. Jiang, *Prog. Photovoltaics Res. Appl.*, 2025, **33**, 795–810.

57 Z. Zhang, W. Chen, X. Jiang, J. Cao, H. Yang, H. Chen, F. Yang, Y. Shen, H. Yang, Q. Cheng, X. Chen, X. Tang, S. Kang, X.-m. Ou, C. J. Brabec, Y. Li and Y. Li, *Nat. Energy*, 2024, **9**, 592–601.

58 R. Lin, Y. Wang, Q. Lu, B. Tang, J. Li, H. Gao, Y. Gao, H. Li, C. Ding, J. Wen, P. Wu, C. Liu, S. Zhao, K. Xiao, Z. Liu, C. Ma, Y. Deng, L. Li, F. Fan and H. Tan, *Nature*, 2023, **620**, 994–1000.

59 J. Wang, Z. Zheng, P. Bi, Z. Chen, Y. Wang, X. Liu, S. Zhang, X. Hao, M. Zhang, Y. Li and J. Hou, *Natl. Sci. Rev.*, 2023, **10**, nwad085.

60 J. Wang, L. Zeng, D. Zhang, A. Maxwell, H. Chen, K. Datta, A. Caiazzo, W. H. M. Remmerswaal, N. R. M. Schipper, Z. Chen, K. Ho, A. Dasgupta, G. Kusch, R. Ollearo, L. Bellini, S. Hu, Z. Wang, C. Li, S. Teale, L. Grater, B. Chen, M. M. Wienk, R. A. Oliver, H. J. Snaith, R. A. J. Janssen and E. H. Sargent, *Nat. Energy*, 2024, **9**, 70–80.

61 S. Liu, Y. Lu, C. Yu, J. Li, R. Luo, R. Guo, H. Liang, X. Jia, X. Guo, Y.-D. Wang, Q. Zhou, X. Wang, S. Yang, M. Sui, P. Müller-Buschbaum and Y. Hou, *Nature*, 2024, **628**, 306–312.